Hindawi

Research Article

Entropy Minimization on Sutterby Nanofluid past a Stretching Surface with Swimming of Gyrotactic Microorganisms and Nanoparticles

F. Ali [ID],[1] **K. Loganathan** [ID],[2,3] **E. Prabu** [ID],[4] **S. Eswaramoorthi** [ID],[5] **M. Faizan** [ID],[1] **A. Zaib,**[1] **and Dinesh Kumar Chaudhary** [ID][6]

[1]*Department of Mathematical Sciences, Federal Urdu University of Arts, Sciences & Technology, Gulshan-e-Iqbal, Karachi 75300, Pakistan*
[2]*Department of Mathematics and Statistics, Manipal University Jaipur, Jaipur-303007, Rajasthan, India*
[3]*Research and Development Wing, Live4Research, Tiruppur 638106, Tamilnadu, India*
[4]*Department of Mathematics, Erode Arts and Science College, Erode, Tamilnadu, India*
[5]*Department of Mathematics, Dr. N. G. P. Arts and Science College, Coimbatore, Tamilnadu, India*
[6]*Department of Physics Amrit Campus, Tribhuvan University, Kathmandu, Nepal*

Correspondence should be addressed to K. Loganathan; loganathankaruppusamy304@gmail.com and Dinesh Kumar Chaudhary; din.2033@gmail.com

This analysis examines the flow of Sutterby nanofluid having bioconvection due to a stretching sheet and heated convective boundary condition. The heat sink/source was imposed in terms of the energy equation. The entropy minimization is also considered. Through the appropriate transformation of the system of nonlinear PDE's setting, the existing problem has altered into nonlinear ODEs and then numerically utilized via the bvp4c method. The numerical values of skin friction, Nusselt number, Sherwood number, and motile density profiles are revealed in a tabular form. In comparison, other governing variables on velocity, temperature, concentration, and bioconvection are seen through various plots and discussed. For example, increment in the Deborah number of heat flux depreciated in temperature distribution while opposite observation was carried out for heat source and sink parameter. Moreover, it has also been investigated that the shear-thinning fluid is entirely reverse to that of the shear thickening fluid. Further, the increase in the magnetic number accelerates in the Bejan number and irreversibility ratio. Finally, the comparison has been made with previous literature and found an excellent agreement.

1. Introduction

The non-Newtonian fluid flow past the stretching surface has massive features in science and engineering technology. Various kinds of non-Newtonian fluid models are paid widely remarkable attention due to their outstanding features such as polymers solution, multiple types of engine oil, and paint. The power-law model has been achieved by the rheological properties of complex fluids such as oil and polymer solution. Sutterby fluid model [1, 2] validates the phenomenon of pseudoplastic and dilatants and obtains comprehensive

mathematical expression. The hyperbolic tangent flow with the Dufour effect due to stretching surface was attempted by Gangadhar et al. [3]. MHD flow of Sutterby fluid in a Darcy surface has been conducted by Bilal et al. [4]. The thermal behavior of Sutterby nanomaterial with stratification is discussed by Nazeer and others [5]. Khan et al. [6] described Sutterby nanofluid over a rotating disk. The combined effect of heat and mass transfer in the MHD flow of Sutterby nanoliquid due to stretching cylinder is deliberated by Sohail and Naz [7]. Rehman and others [8] reported the thermal stratification phenomenon on the Sutterby nanofluid with zero mass flux

condition. The significance of heat and mass transfer on Sutterby nanofluid past a wedge surface was discussed by Usman and others. [9]. Bhatti [10] et al. reported the chemically reactive mass transport mechanism on the Jeffrey fluid model in the presence of extrinsic magnetic impact discussed in this paper. A permeable material is used to move the fluid. The mathematical modeling of momentum and concentration equations is done via Lie group transformations. Loganathan et al. [11] conducted a steady flow of thermal analysis of Oldroyd-B flow under second-order slip and cross-diffusion effects.

In the last few decades, nanofluid established the contemplation of numerous researchers because of their various industrial and mechanical engineering applications. It is also observed that heat transport fluids efficiently depend on their physical distinctiveness, such as thermal conductivity. There are a few base fluids containing water, oil, ethylene, and many more that have less conductivity. As a result, such types of liquids have deprived heat transfer phenomena. So, enhancing their thermal conductivity needs to be an important problem to receive the views of recent scholars. The word nanofluid was employed by [12], which showed thermal performance. Later, to augment the thermal properties of nanofluid, Buongiorno [13] added two main features of nanoliquid, namely, Brownian movement and thermophoretic. The MHD flow of micropolar nanomaterial between two rotating surfaces has been designed by Islam et al. [14]. Nonlinear radiation, swimming microorganisms, and nanoparticles with a 3D bioconvective viscoelastic nanofluid flow across a heated Riga surface were studied by Karthik et al. [15]. Ijaz et al. [16] studied the radiative flow of Sisko nanofluid over a stretching rotating circle with entropy generation. The impact of nanofluid characteristics and heat exchange inside a twisted tube over a revolving disk is pointed out by Alempour et al. [17]. The research by Abo-Elkhair et al. [18] looks at the effects of magnetic force and nonlinear thermal radiation on hybrid bio-nanofluid flow in a peristaltic channel under the influence of a high and low Reynolds number applied magnetic field. Sabir et al. [19] introduced the influence of thermal radiative on Sutterby nanofluid by using Cattaneo-Christov heat near the stagnation point. Ali and Zaib [20] studied time-dependent Eyring-Powell comprising nanoliquid due to convective conditions. Khan et al. [21] looked at the effect of heat and mass transport on third-grade nanofluid due to heat convectively stretching sheet. Ibrahim and Makinde [22] considered the power-law nanofluid over convective boundary conditions near the stagnation point. Bhatti et al. [23] address the nanofluid flow and microbe swimming across parallel rotating circular plates separated by a limited distance and containing a porous media.

In the past few years, numerous analyses into energy creation in various fluid stream conditions have been taken out by investigators' attention on the entropy generation. Many investigators are stimulated by recognizing the features of entropy production in liquid flow and some applications such as heat pumps, fire engines, air conditioners, and many more. The entropy production minimization had been coined by Bejan [24]. Later, the impact of entropy production on the Sutterby nanofluid past a stretching surface near the stagnation point was discovered by Azhar et al. [25]. Hayat et al. [26] discussed the MHD peristaltic flow of Sutterby nanofluid and

entropy generation. Loganathan et al. [27] examined the third-grade nanofluid flow over a stretching plate with entropy generation. They found that, for the higher thermal relaxation time parameter, the entropy production and Bejan number profiles show the opposite impact. Furthermore, the radiation constant, Biot number, suction/injection constant, Hartmann number, and Brinkman number all improve the system's entropy. Yousaf and others [28] explained the influence of entropy optimization and motile density of Williamson nanofluid past an inclined sheet. Makinde and Tshehla [29] deliberated the mixed convective flow of nanoliquid in an entropy minimization and mass suction/injection. Loganathan and Rajan [30] presented the Williamson nanofluid flow with zero mass flux and Joule heating impacts. They also found the entropy generation of the problem. Afridi et al. [31] considered Newtonian flow for entropy minimization induced by the thermal radiative flow. Inside the cavity, the entropy production of fluid flow with the permeable surface is scrutinized by Alsabery [32].

Sutterby fluid [1, 2] is one of the very important non-Newtonian fluids which shows the modeled equations of high polymer aqueous solution. The current analysis is dedicated to inspecting the entropy production on bioconvection for the flow of Sutterby fluid because a heated convective sheet is examined. Thermal radiation, heat sink/source, Brownian motion, and thermophoresis are also considered. The main aim of this study is that the non-Newtonian Sutterby fluid is selected to examine the rheological properties of shear-thinning/thickening with the effect of thermal radiation and microorganism. The similarity conversion is used to alter the nonlinear PDE into ODE to solve modeled equations. The numerical solution of these modeled equations has been produced via BVP4c in Matlab. To investigate the behavior of velocity, temperature, concentration, and motile density, they are plotted against numerous variables. The numerical computation is displayed in the form of figures and tables. Manufacturing of rubber and plastic sheets, melt-spinning, glass-fiber manufacturing, and metallic plate cooling systems are some of the beneficial uses of this sort of inquiry. Also, the Bejan number is used to estimate entropy generation in power engineering and aeronautical propulsion to forecast the smartness of the overall system.

1.1. Mathematical Formulation.

The incompressible, laminar, time-dependent flow of Sutterby nanomaterial past stretching sheet subject to the convective condition and entropy production is examined. The stretching sheet velocity is $U_w(x, t) = ax/1 - \gamma t$. The mathematical modeling of the physical problem is designed with coordinate (x, y) with velocity component $(\widehat{u}, \widehat{v})$ taken in x- and y-axis (see Figure 1). The mathematical formulation for Sutterby nanofluid in a steady flow is taken in [25], and it converted to be unsteady in the following flow equations.

$$\frac{\partial \widehat{u}}{\partial x} + \frac{\partial \widehat{v}}{\partial y} = 0, \tag{1}$$

$$\frac{\partial \widehat{u}}{\partial t} + \widehat{u}\frac{\partial \widehat{u}}{\partial x} + \widehat{v}\frac{\partial \widehat{u}}{\partial y} = \frac{\mu_0}{\rho}\left[\frac{\partial^2 \widehat{u}}{\partial y^2} + \frac{mB^2}{2}\left(\frac{\partial \widehat{u}}{\partial y}\right)^2\frac{\partial^2 \widehat{u}}{\partial y^2}\right] - \frac{\sigma}{\rho}B_0^2\widehat{u}, \tag{2}$$
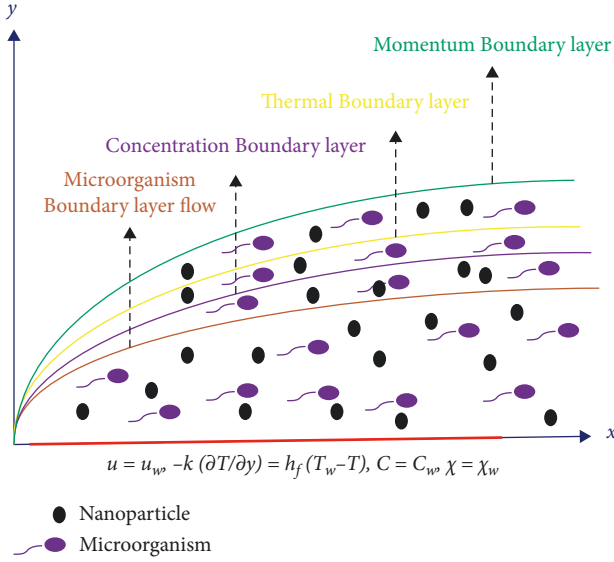
FIGURE 1: Physical model.

$$\frac{\partial \widehat{T}}{\partial t} + \widehat{u}\frac{\partial \widehat{T}}{\partial x} + v\frac{\partial \widehat{T}}{\partial y} = \frac{k}{\rho C_p}\left(\frac{\partial^2 \widehat{T}}{\partial y^2}\right)$$

$$+ \tau\left(D_B\frac{\partial \widehat{C}}{\partial y}\frac{\partial \widehat{T}}{\partial y} + \frac{D_T}{\widehat{T}_\infty}\left(\frac{\partial \widehat{T}}{\partial y}\right)^2\right) \quad (3)$$

$$- \frac{1}{\rho C_p}\frac{\partial q_r}{\partial y} + \frac{Q_0}{\rho C_p}\left(\widehat{T} - \widehat{T}_\infty\right),$$

$$\frac{\partial \widehat{C}}{\partial t} + \widehat{u}\frac{\partial \widehat{C}}{\partial x} + \widehat{v}\frac{\partial \widehat{C}}{\partial y} = D_B\frac{\partial^2 \widehat{c}}{\partial y^2} + \frac{D_T}{\widehat{T}_\infty}\left(\frac{\partial^2 \widehat{T}}{\partial y^2}\right) - \kappa_0\left(\widehat{C} - \widehat{C}_\infty\right),$$

(4)

$$\frac{\partial \widehat{\chi}}{\partial t} + \widehat{u}\frac{\partial \widehat{\chi}}{\partial x} + \widehat{v}\frac{\partial \widehat{\chi}}{\partial y} + \frac{bW_c}{\left(\widehat{C}_w - \widehat{C}_\infty\right)}\frac{\partial}{\partial y}\left(\widehat{\chi}\frac{\partial \widehat{C}}{\partial y}\right) = D_m\frac{\partial^2 \widehat{\chi}}{\partial y^2}. \quad (5)$$

With boundary condition,

$$\widehat{u} = U_w(x,t), \widehat{v} = 0, -k\frac{\partial \widehat{T}}{\partial y} = h(t)\left(\widehat{T}_w - \widehat{T}_\infty\right),$$

$$\widehat{C} = \widehat{C}_w, \widehat{\chi} = \widehat{\chi}_w \ y = 0,$$

$$\widehat{u} \longrightarrow 0, \widehat{T} \longrightarrow \widehat{T}_\infty, \widehat{C} \longrightarrow \widehat{C}_\infty, \widehat{\chi} \longrightarrow \widehat{\chi}_\infty \ at \ y \longrightarrow \infty.$$

(6)

In equation (2), m shows three conditions. If $m < 0$, then it shows pseudoplastic or represents fluid with decreasing viscosity; if $m > 0$, it demonstrates the dilatant or fluid with increasing viscosity; if $m = 0$, it reflects the Newtonian fluid.

The Rosseland approximation is crucial in thermal radiative heat flow. The Rosseland approximation requires an optically thick medium and radiation that travels only a short distance before being scattered or absorbed. As a result, a simplified model for the Radiative Transfer Equation (RTE) based on the Rosseland approximation is provided as follows:

$$q_r = \frac{4\sigma_1}{3k*}\frac{\partial \widehat{T}^4}{\partial y} = -\frac{16\sigma^*}{3k^*}\widehat{T}^3\frac{\partial \widehat{T}^4}{\partial y}, \quad (7)$$

where $\widehat{T}^4$ can be expanded as follows:

$$\widehat{T}^4 \cong 4\widehat{T}_\infty^3\widehat{T} - 3\widehat{T}_\infty^4. \quad (8)$$

Replacing equation (7) into equation (8),

$$q_r = \frac{16\sigma * T_\infty^3}{3k*}\frac{\partial \widehat{T}}{\partial y}. \quad (9)$$

Similarity expressions are

$$\widehat{u} = \frac{ax}{1-\gamma t}f'(\eta), \widehat{v} = -\sqrt{\frac{av}{1-\gamma t}}f(\eta), \eta = \sqrt{\frac{a}{v(1-\gamma t)}}y,$$

$$\theta = \frac{\widehat{T} - \widehat{T}_\infty}{\widehat{T}_w - \widehat{T}_\infty}, \phi = \frac{\widehat{C} - \widehat{C}_\infty}{\widehat{C}_w - \widehat{C}_\infty}, N = \frac{\widehat{\chi} - \widehat{\chi}_\infty}{\widehat{\chi}_w - \widehat{\chi}_\infty},$$

(10)

$$f''' + ff'' - f'^2 - A\left(f' + \frac{\eta}{2}f''\right) + \frac{1}{2}m\delta\mathrm{Re}f''^2f'' + Mf' = 0,$$

(11)

$$\theta''\left(1 + \frac{4}{3}Rd\right) - \mathrm{Pr}\frac{1}{2}\eta A\theta' + \mathrm{Pr}\,Nt\theta'^2 + \mathrm{Pr}\,Nb\theta'\phi' + \mathrm{Pr}\,\varepsilon\,\theta = 0,$$

(12)

$$\phi'' + Sc(f\phi') - \frac{1}{2}\eta ScA\phi' + \left(\frac{Nb}{Nt}\right)\theta'' - Sc\kappa\phi = 0, \quad (13)$$

$$N'' - Pe\left[\phi''(N + \varpi) + \phi'N'\right] - Lb\left(\frac{1}{2}\eta AN' + fN'\right) = 0.$$

(14)

The converted boundary conditions are

$$f(0) = 0, f'(0) = 1, \theta'(0) = -Bi + Bi(\theta(0)), \phi(0) = 1$$
$$f'(\infty) = 0, \theta(\infty) = 0, \phi(\infty) = 0, N(\infty) = 0.$$

(15)

The Reynolds number ($\mathrm{Re} = ax^2/v$), Deborah number ($\delta = B^2a^2/v$), magnetic parameter ($M = \sigma B_0^2/\rho a$), unsteady parameter ($A = \gamma/a$), heat source parameter (ε), radiation parameter ($Rd = (4\sigma^*T_\infty^3)/(kk^*)$), Prandtl number ($\mathrm{Pr} = v/\alpha$), Brownian motion parameter ($Nb = \tau D_B(\widehat{C}_w - \widehat{C}_\infty)/v$), thermophoresis parameter ($Nt = \tau D_T(\widehat{T}_w - \widehat{T}_\infty)/\widehat{T}_\infty v$), Schmidt number ($Sc = v/D_B$), Biot number ($Bi = d/k\sqrt{v/a}$), microorganisms concentration ($\varpi = \widehat{\chi}_\infty/\widehat{\chi}_m - \widehat{\chi}_\infty$), Bioconvection Peclet number ($Pe = bW_c/D_m$). Bioconvection Lewis number ($Lb = v/D_m$) are shown.

2. Engineering Interest Quantities

$$C_{fx} = \frac{\tau_w}{\rho u_w^2}, \; Nu_x = \frac{xq_w}{k(\widehat{T}_w - \widehat{T}_\infty)},$$

$$Sh_x = \frac{xq_m}{D_b(\widehat{C}_w - \widehat{C}_\infty)}, \tag{16}$$

$$Nn = \frac{xq_n}{D_m(\widehat{\chi}_w - \widehat{\chi}_\infty)}.$$

Shear wall τ_w, heat q_w, mass q_m, and motile density q_n have been displayed as

$$\tau_w = -\mu_0 \left[\frac{\partial \widehat{u}}{\partial y} + \frac{m}{6} \text{Re} \; \delta \left(\frac{\partial \widehat{u}}{\partial y} \right)^3 \right]_{y=0}$$

$$q_w = -k \left(\frac{\partial \widehat{T}}{\partial y} \right) \Big|, \; q_m = -k \left(\frac{\partial \widehat{C}}{\partial y} \right) \Big|_{y=0},$$

$$q_n = -D_m \left(\frac{\partial \widehat{\chi}}{\partial y} \right) \Big|_{y=0}. \tag{17}$$

In the use of (10) and (17),

$$C_f \text{Re}_x^{0.5} = \left[f''(0) + \frac{m}{6} \delta \, \text{Re} \left(f''(0) \right)^3 \right],$$

$$\frac{Nu_x}{\text{Re}_x^{1/2}} = -\theta'(0) \left[1 + \frac{4}{3} Rd \right],$$

$$\frac{Sh_x}{\text{Re}_x^{1/2}} = -\phi'(0), \; \frac{Nn}{\text{Re}_x^{1/2}} = -N'(0). \tag{18}$$

3. Entropy Generation Analysis

The entropy production rate (S_G) for the Sutterby fluid [25] under magnetic field, thermal radiation, and diffusion effect can be written as

$$S_G = \frac{k}{\widehat{T}_0} \left(\left[\frac{\partial \widehat{T}}{\partial x} \right]^2 + \left[\frac{\partial \widehat{T}}{\partial y} \right]^2 + + \frac{16\sigma^* \widehat{T}_\infty^3}{3kk^*} \left(\frac{\partial \widehat{T}}{\partial y} \right)^2 \right) + \frac{\mu}{\widehat{T}_\infty} \left(\frac{\partial \widehat{u}}{\partial y} \right)^2 \left[1 + \frac{m\text{Re}\delta}{6} \left(\frac{\partial \widehat{u}}{\partial y} \right)^2 \right] + \frac{RD_m}{\widehat{C}_\infty} \left(\frac{\partial \widehat{C}}{\partial y} \right)^2$$

$$+ \frac{RD_m}{\widehat{T}_\infty} \left(\frac{\partial T}{\partial y} \right) \left(\frac{\partial \widehat{C}}{\partial y} \right) + \frac{RD_m}{\widehat{\chi}_\infty} \left(\frac{\partial \widehat{\chi}}{\partial y} \right)^2 + \frac{RD_m}{\widehat{T}_\infty} \left(\frac{\partial \widehat{\chi}}{\partial y} \right) \left(\frac{\partial \widehat{T}}{\partial y} \right) + \frac{\sigma B_0^2}{\widehat{T}_\infty} u^2. \tag{19}$$

The dimensionless entropy generation number is expressed as

$$Ns = (1 + R \, d)\theta'^2 + \text{Re} \frac{Br}{\Pi} \left[1 + \frac{m\text{Re}\delta}{3} (f'')^2 \right] (f'')^2 + \text{Re} \left(\frac{\Gamma}{\Pi} \right)^2 \phi'^2$$

$$+ \text{Re} \left(\frac{\Gamma}{\Pi} \right) \phi' \theta' + \text{Re} \left(\frac{\xi}{\Pi} \right)^2 N'^2 + \text{Re} \left(\frac{\xi}{\Pi} \right) N' \theta' + \frac{Br}{\Pi} M \, f'^2. \tag{20}$$

The Bejan number (Be) is described as

$$Be = \frac{(1 + R \, d)\theta'^2 + \text{Re} \, (\Gamma/\Pi)^2 \phi'^2 + \text{Re} \, (\Gamma/\Pi)\phi'\theta' + \text{Re} \, (\xi/\Pi)^2 N'^2 + \text{Re} \, (\xi/\Pi)N'\theta'}{(1 + Rd)\theta'^2 + \text{Re} \, Br/\Pi \left[1 + m\text{Re}\delta/3 (f'')^2 \right] (f'')^2 + \text{Re} \, (\Gamma/\Pi)^2 \phi'^2 + \text{Re} \, (\Gamma/\Pi)\phi'\theta' + \text{Re} \, (\xi/\Pi)^2 N'^2 + \text{Re} \, (\xi/\Pi)N'\theta' + Br/\Pi M \, f'^2}. \tag{21}$$

3.1. Solution Methodology. To compute the numeric outcomes of formulated systems of ODEs (10)–(13) subject to boundary conditions equation (14) by bvp4c technique, the ODEs are renovated into first-order ODEs by assigning a new variable.

$$
\left.
\begin{aligned}
&f = \Upsilon_1, f' = \Upsilon_2, f'' = \Upsilon_3, f''' = \Upsilon_3' \\
&\theta = \Upsilon_4, \theta' = \Upsilon_5, \theta'' = \Upsilon_5' \\
&\phi = \Upsilon_6, \phi' = \Upsilon_7, \phi'' = \Upsilon_7' \\
&N = \Upsilon_8, N' = \Upsilon_9, N'' = \Upsilon_9'
\end{aligned}
\right\},
\tag{22}
$$

$$
\Upsilon_3' = \frac{\left\{-\Upsilon_1\Upsilon_3 + (\Upsilon_2)^2 - M\Upsilon_2\right\}}{\left[1 + 1/2m\delta \ \mathrm{Re}\Upsilon_3^2\right]},
\tag{23}
$$

$$
\Upsilon_5' = \frac{\left[-\mathrm{Pr}\Upsilon_1\Upsilon_5 + \alpha\Upsilon_1\Upsilon_2\Upsilon_5 - \mathrm{Pr}\left(Nb\Upsilon_5\Upsilon_7 + Nt\Upsilon_5^2\right)\right]}{\left(1 + R\ d - \alpha\Upsilon^2\right)},
\tag{24}
$$

$$
\Upsilon_7' = -\left[ScSr\Upsilon_5' - Sc\Upsilon_1\Upsilon_5 + \Upsilon_5'\frac{Nt}{Nb} - Sc\ \kappa\Upsilon_6\right],
\tag{25}
$$

$$
\Upsilon_9' = Pe\Upsilon_7'(\Upsilon + \varpi) - \Upsilon_7\Upsilon_9 + Lb\Upsilon_9.
\tag{26}
$$

The converted boundary condition is

$$
\begin{aligned}
&\Upsilon_1(0) = 0, \Upsilon_2(0) = 1, \Upsilon_5(0) = -\gamma(1 - \Upsilon_4(0)), \Upsilon_6(0) \\
&\quad = 1, \Upsilon_8(0) = 1
\end{aligned}
\tag{27}
$$
$$
\Upsilon_2(\infty) = 0, \Upsilon_4(\infty) = 0, \Upsilon_6(\infty) = 0, \Upsilon_8(\infty) = 0.
$$

By using (27) with boundary conditions, the results are using a finite value for η_{max} .

$$
\begin{aligned}
&f\prime(\eta_{\max}) \longrightarrow 0, \theta(\eta_{\max}) \longrightarrow 0, \phi(\eta_{\max}) \\
&\quad \longrightarrow 0, N(\eta_{\max}) \longrightarrow 0.
\end{aligned}
\tag{28}
$$

The step size is measured $\Delta\eta = 0.001$ and 10^{-6} is a convergent criterion to repeat and attain the numeric solution.

4. Result and Discussion

The current study involves the governing parameters on velocity $f'(\eta)$, temperature $\theta(\eta)$, concentration $\theta(\eta)$, density of motile microorganisms $N(\eta)$, entropy generation $Ns(\eta)$, and Bejan number $Be(\eta)$. Table 1 presents the code validation of $-\theta(0)$ for different Pr values. This validation provides that the result of our computation is an optimum one.

Figures 2(a)–2(d) delineate the different values of the Deborah number (δ) on velocity distribution $f'(\eta)$, temperature field $\theta(\eta)$, entropy generation $Ns(\eta)$, and Bejan number $Be(\eta)$. Figure 2(a) presents the larger value of the Deborah number (δ) results, the fluid velocity reduces for pseudoplastic flow $(m < 0)$, and fluid velocity enhances as the Deborah number δ upsurges for the

dilatant flow $(m < 0)$. The Deborah number fluidity for scenarios when $m > 0$ and $m < 0$ is represented. In both circumstances, increasing the value of the Deborah number results in the opposite behavior of the velocity fields. The flow of fluid accelerates as the Deborah number increases but decreases as the Deborah number increases in the form of the pseudoplastic fluid. Increases in the values of the Deborah number play an important part in refining elastic impacts, and as a result, dilatant fluids increase fluid flow; nevertheless, the pseudoplastic fluid exhibits quite different behavior. An increment in the value of the Deborah number as thermal layer thickness depreciates for pseudoplastic flow $(m < 0)$ in Figure 2(b). Also, the temperature field $\theta(\eta)$ reduces with the increasing value of the Deborah number δ in the shear thickening fluid $(m < 0)$. Figures 2(c) and 2(d) interestingly show that entropy production rate $Ns(\eta)$ enhances for dilatant $(m < 0)$ and reduces for pseudoplastic $(m < 0)$ through the escalation in the Deborah parameter δ while the Bejan number $Be(\eta)$ is an escalating function of the Deborah number (δ) for both pseudoplastic flow $(m < 0)$ but reduces dilatant flow $(m < 0)$. The plot of various values of power-law index parameter (m) is shown in Figures 3(a) and 3(b). In Figure 3(a), the velocity profile $f'(\eta)$ escalates as (m) rises. Moreover, the velocity profile $f'(\eta)$ is interpreted through (m=0, m<0, m>0). The Newtonian fluid $(m = 0)$, pseudoplastics $(m < 0)$, and dilatants fluid $(m < 0)$ are analyzed. The Newtonian, shear-thinning, and shear-thickening fluid is described in Figure 3(b). The temperature profile $\theta(\eta)$ decays with a larger value of m. Figures 4(a)–4(d) display the behavior of unsteady variable A on $f'(\eta)$, $\theta(\eta)$, $Ns(\eta)$, and $Be(\eta)$. For both cases $m > 0$ and $m < 0$, Figures 4(a) and 4(b) represent that both velocity and temperature profiles decay due to greater value of A. Actually, the unsteady variable reduces the flow strength of velocity profile $f'(\eta)$ and temperature field $\theta(\eta)$. The reason behind this is that pseudoplastic and dilatant fluid was not affected on both profiles. Similar performance for $Ns(\eta)$ and $Be(\eta)$ was noted in Figures 4(c) and 4(d).

Figures 5(a)–5(d) depict the feature of (Re) for the velocity distribution $f'(\eta)$, temperature field $\theta(\eta)$, entropy generation $Ns(\eta)$, and Bejan number $Be(\eta)$. From Figure 5(a), the arising value of the Reynolds number (Re) diminishes the velocity profile $f'(\eta)$ for viscous force and velocity field augment due to the larger value of the Reynolds number for dilatant fluid. Figure 5(b) shows that a larger value of the Reynolds number (Re) causes a reduction in temperature profile for shear-thinning and temperature profile decreases as there is an increment in (Re). Figures 5(c) and 5(d) display that both entropy minimization and the Bejan number reduce and upsurge with the rise of the value of Re. The plots of the magnetic variable on the velocity and temperature profiles are exposed in Figure 6(a)–6(d). The velocity of the fluid grows with a mounting value of M while an opposite observation is noted for the temperature field for both $(m < 0)$ and $(m < 0)$. Physically, there is an increment in the strength of the magnetic field whereas resistive force turned down the velocity. From Figure 6(c), the entropy minimization increases with a larger magnitude

TABLE 1: Comparing of $-\theta(0)$ for the diverse value of the Prandtl number Pr.

Pr	Goyal and Bhargava [33] (FEM)	G. B. Chandra Mouli et al. [34]	Current solution
0.7	0.4539	0.45391616	0.456051151444
2	0.9113	0.91135768	0.911321182335
7	1.8954	1.89540326	1.895381877516
20	3.3539	3.35390035	3.353886926545
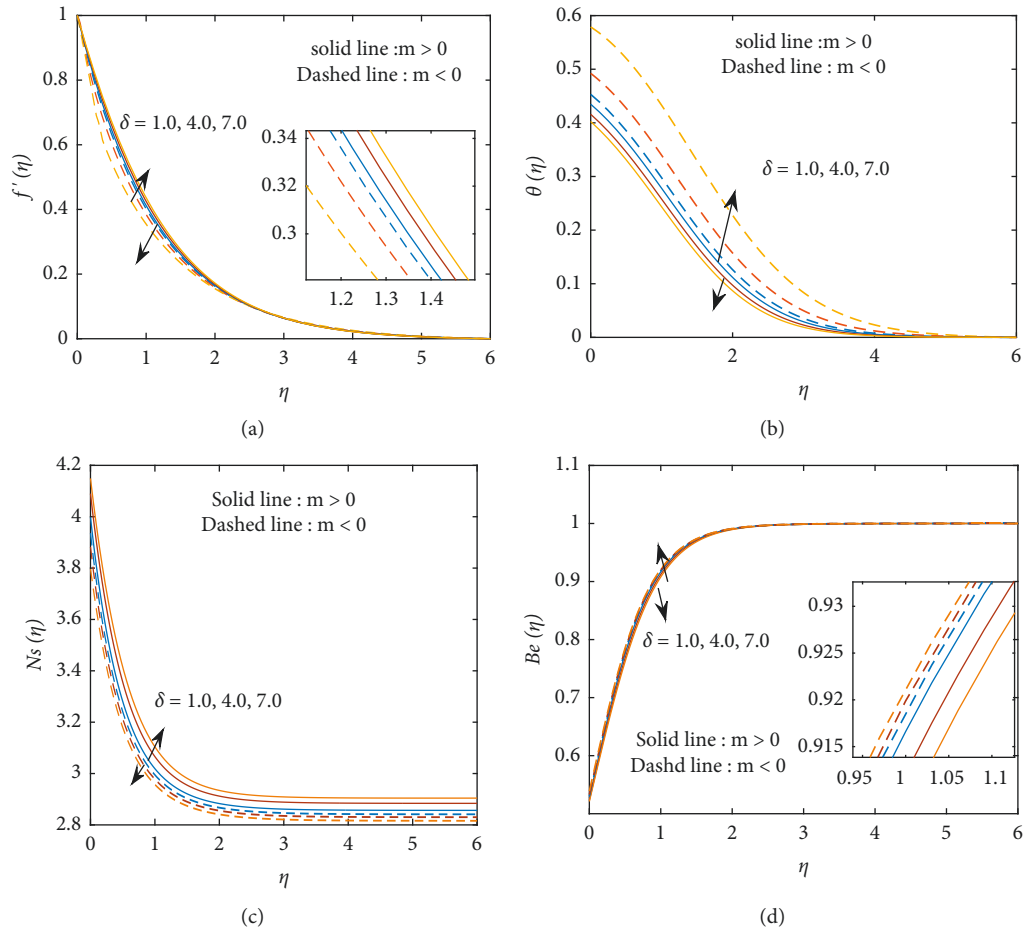
FIGURE 2: Impact of δ on (a) $f'(\eta)$, (b) $\theta(\eta)$, (c) $Ns(\eta)$, and (d) $Be(\eta)$.

of magnetic number for both cases pseudoplastic and dilatants whereas its opposite behavior is seen in Figure 6(d).

The view of (Nb) on temperature field $\theta(\eta)$ and concentration profile $\phi(\eta)$ is disseminated in Figures 7(a) and 7(b). The temperature profile $\theta(\eta)$ is enhanced with enhancing the value of the Brownian motion (Nb). An augment in the (Nb) causes an enhancement in the nanoparticle collision that results in an increment in fluid temperature. However, deceleration in the concentration field is observed in Figure 7(b). Figures 8(a) and 8(b) display thermophoretic estimation (Nt) on temperature $\theta(\eta)$ and concentration profiles $\theta(\eta)$. Larger values of (Nt) for both $\theta(\eta)$ and $\phi(\eta)$ have been intensified. Nanoparticles have dragged from hotter to cold surfaces. That is the reason of the increase in thermal and concentration profiles. The plots for the Prandtl (Pr) and Schmidt number (Sc) on temperature $\phi(\eta)$ and concentration profiles $\phi(\eta)$ are carried out in Figures 9(a) and 9(b). It can be shown from these figures that enlargement in the (Pr) causes a dazzling depreciation in the fluid temperature. The concentration profile reduces with a larger value of (Sc). Physically, the Schmidt number (Sc) is dependent on the proportion of momentum to mass diffusivity. By increasing the value of (Sc), momentum diffusivity increases as nanoparticle concentration declines. Figures 10(a) and 10(b) show the Biot number (Bi) and chemical reaction parameter (κ) on temperature and concentration profiles. The Biot number means the ratio of convection over conduction inside the boundary at the surface. The gradually growing value of values of the Biot number climbs the temperature distribution while similar behavior is observed for increasing value of κ on the concentration profile. The features of the Bioconvection Lewis number (Lb) and Peclet number (Pe) on motile
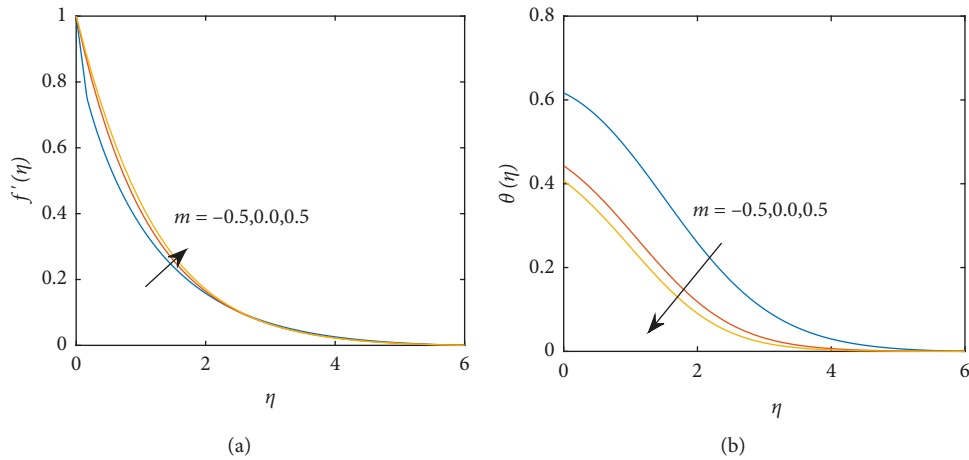
FIGURE 3: Impact of (m) on (a) $f'(\eta)$ and (b) $\theta(\eta)$.
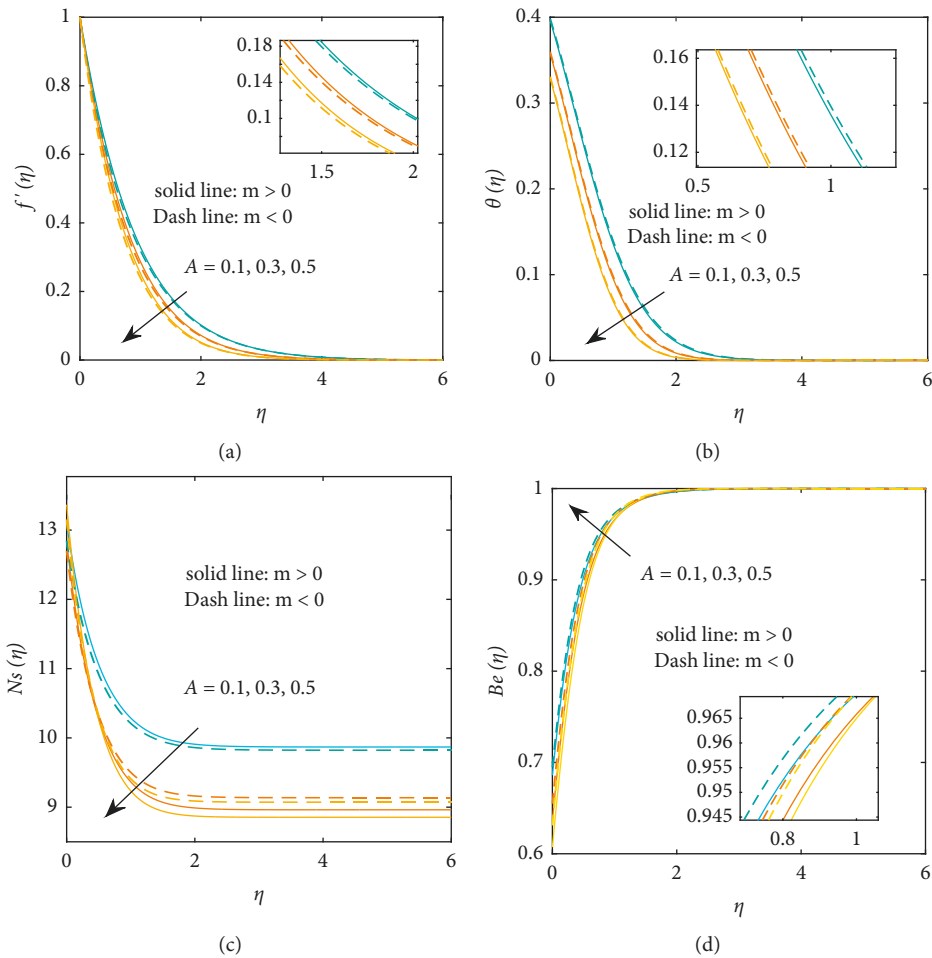

FIGURE 4: Impact of A on (a) $f'(\eta)$, (b) $\theta(\eta)$, (c) $Ns(\eta)$, and (d) $Be(\eta)$.

density microorganism $N(\eta)$ were seen in Figures 11(a) and 11(b). For the mounting value of (Lb) as the diffusivity microorganism upsurges, so, the density of motile microorganism has increased. Figure 11(b) shows the influence of the Peclet number on microorganism density that has been assumed. Enlarging the Peclet number climbs the movement

of fluid particles. Due to this, microorganism density enhances as their concentration diminishes.

The impact of Re and δ on skin friction coefficient was presented in Figure 12 for dilatant and pseudo-plastic cases. In dilatant case, the surface drag force suppresses when enhancing the δ values, and it aggravates for increasing Re

(a)

(b)

(c)

(d)
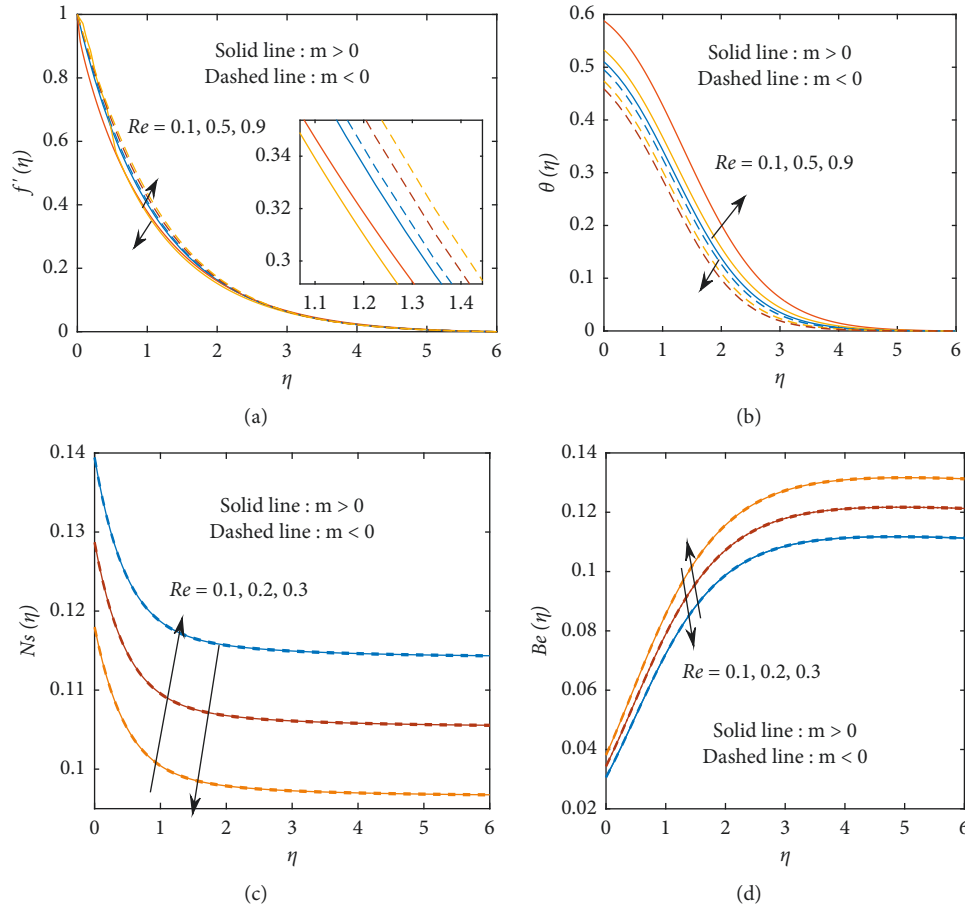
FIGURE 5: Impact of (Re) on (a) $f'(\eta)$, (b) $\theta(\eta)$, (c) $Ns(\eta)$, and (d) $Be(\eta)$.
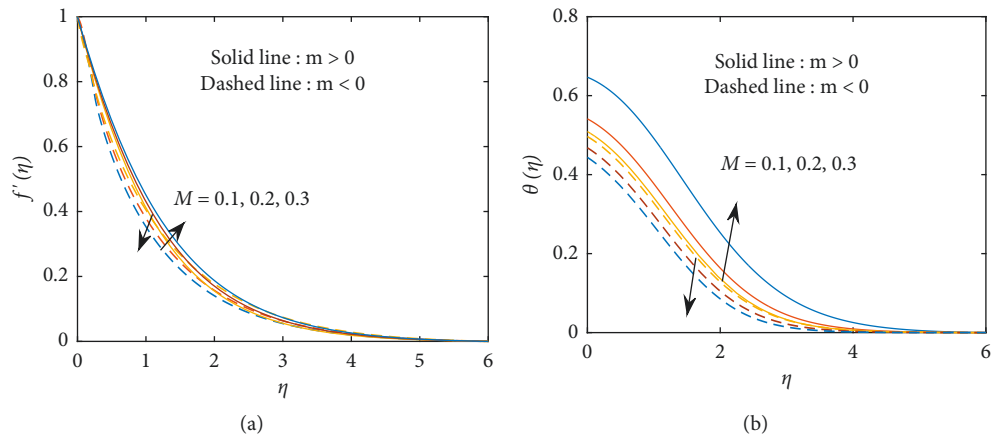

(a)

(b)

FIGURE 6: Continued.

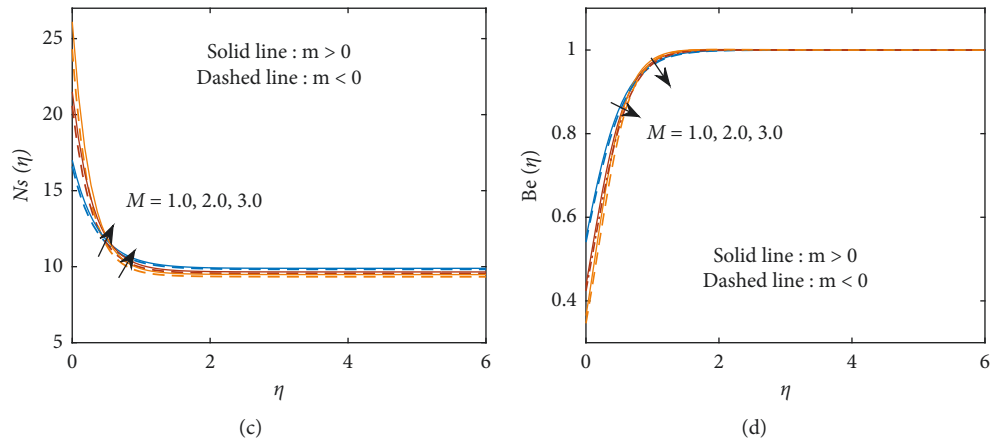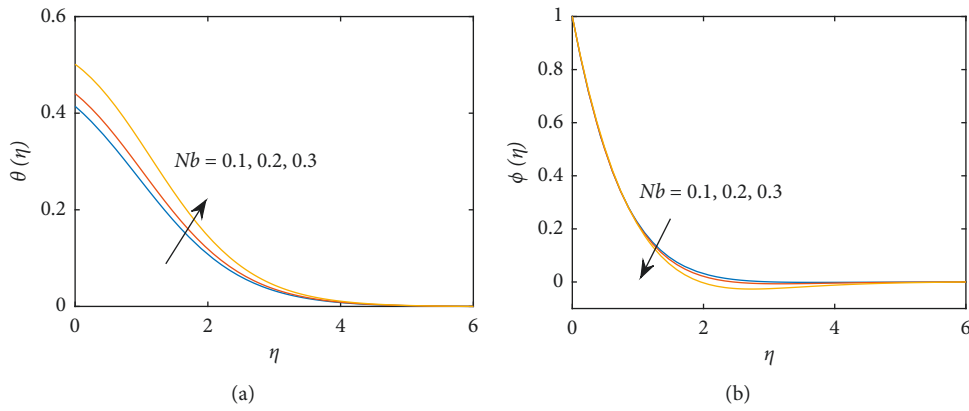FIGURE 6: Impact of M on (a) $f'(\eta)$, (b) $\theta(\eta)$, (c) $Ns(\eta)$, and (d) $Be(\eta)$.

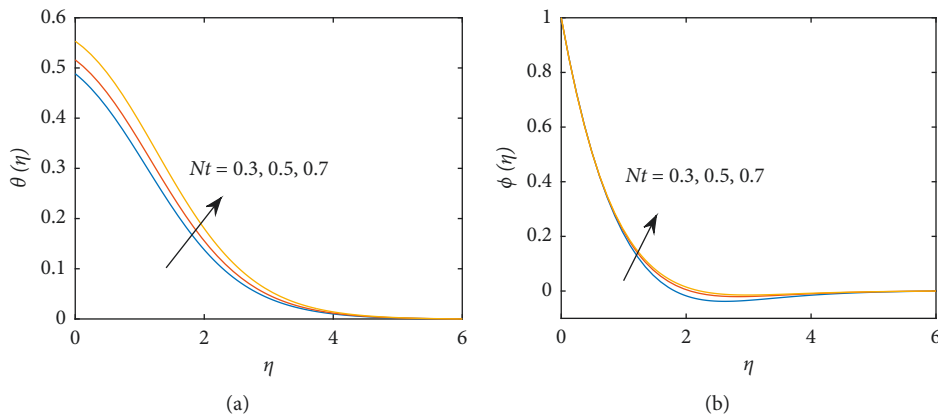FIGURE 7: Impact of Nb on (a) $\theta(\eta)$ and (b) $\phi(\eta)$.

FIGURE 8: Impact of Nt on (a) $\theta(\eta)$ and (b) $\phi(\eta)$.

values and the opposite trend was obtained in pseudo-plastic case. Figure 13 illustrates the variations of Nu for different combinations of Nb and Rd. In small quantity of Nb, the heat transfer gradient upsurges when rising the Rd variations and the reverse trend was attained for higher quantity of Nb. The consequences of κ and Sc on Sherwood number is plotted in

Figure 14. In Sc = 0.8, the Sherwood number enlarges for strengthening the κ values, and the Sherwood number is almost same for changing κ values at Sc = 0.9. In addition, the Sherwood number decays for raising the κ values at Sc = 1.0. Figure 15 gives the impact of Pe and Lb on motile density. It is detected from this figure that the motile density
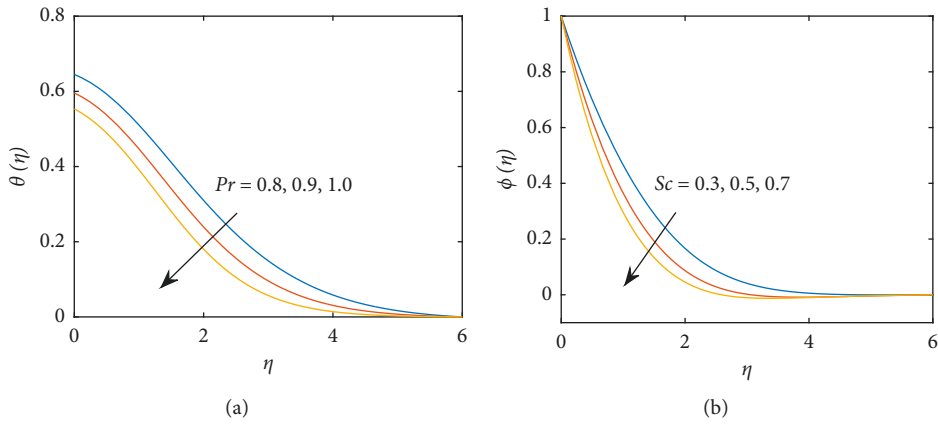
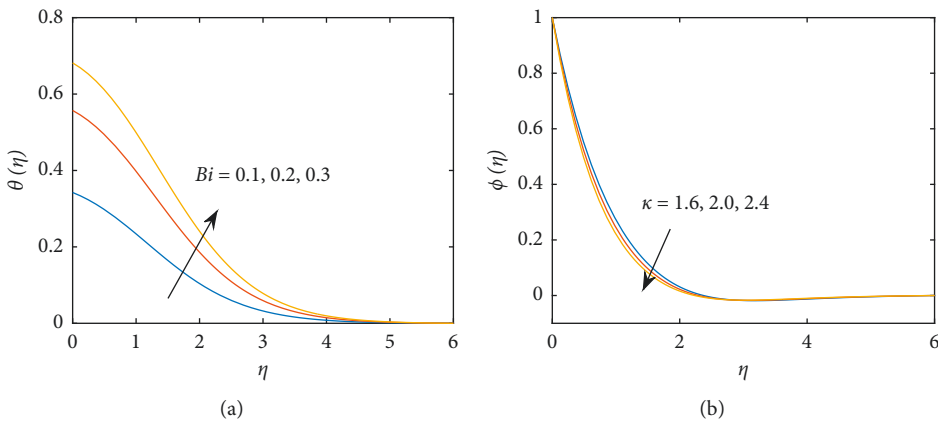FIGURE 9: Impact of Pr on (a) $\theta(\eta)$ and (b) Sc on$\phi(\eta)$.

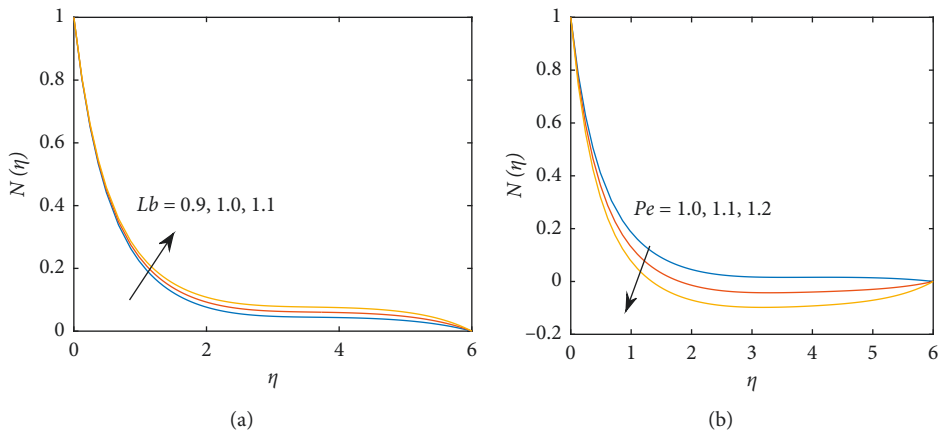FIGURE 10: Impact of (a) Bi on $\theta(\eta)$ and (b) κ on $\phi(\eta)$.

FIGURE 11: Impact of (a) Lb and (b) Pe on $N(\eta)$.

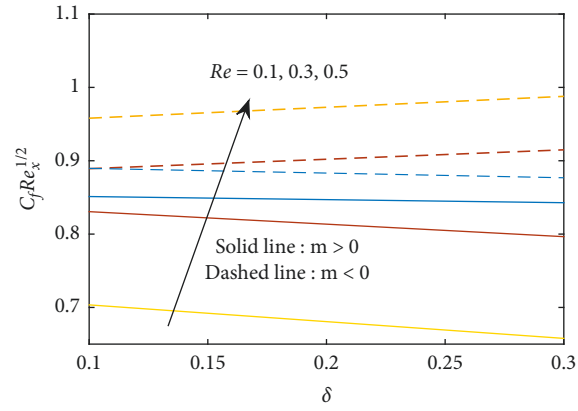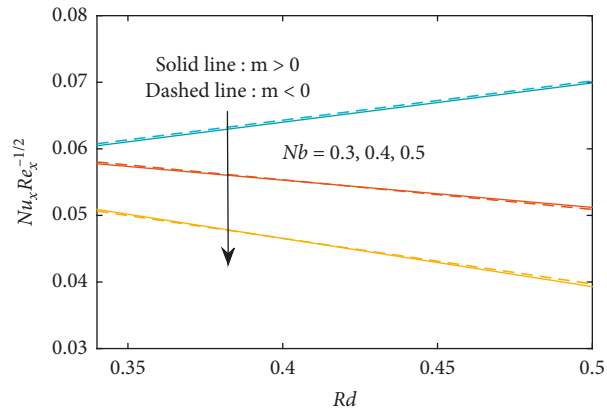FIGURE 12: Impact of Re and δ versus skin friction.

FIGURE 13: Impact of Rd and Nb versus the Nusselt number.
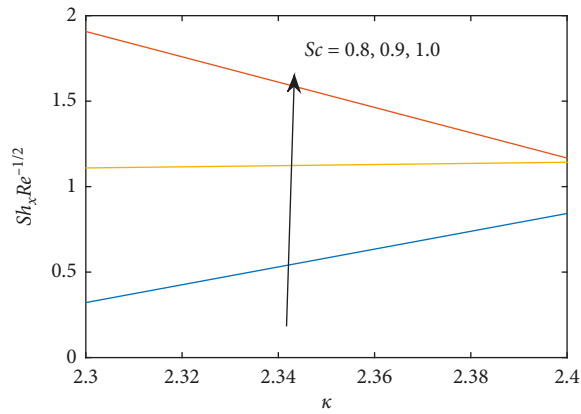

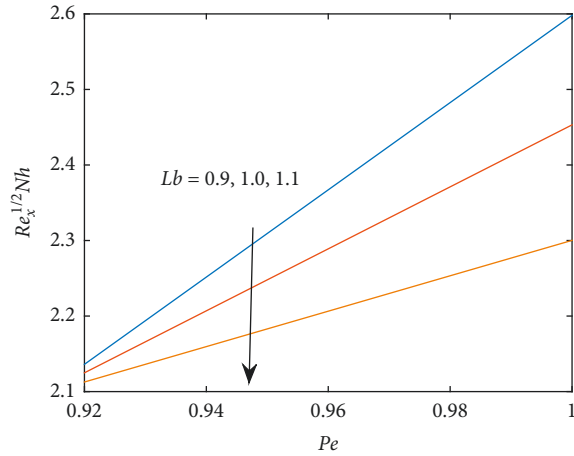FIGURE 14: Impact of κ and Sc versus the Sherwood number.

FIGURE 15: Impact of Lb and Pe versus the Motile density.

TABLE 2: Numerical simulation values of $Re_x^{1/2}Cf_x$ with numerous variables Re, M, δ.

Re	δ	M	$Re_x^{1/2}Cf_x$	
			$m = -0.5$	$m = 0.5$
0.1	0.2	0.2	0.8896	0.8892
0.3			0.8768	0.9149
0.5			0.8638	0.9274
	0.4		0.8306	0.9580
	0.6		0.7965	0.9878
	0.7		0.7790	1.0024
		0.4	0.7035	0.8512
		0.5	0.6578	0.8428
		0.6	0.6943	0.8372

TABLE 3: Numerical values of $Re_x^{-1/2}Nu_x$ with numerous variables of $Rd, Nb, Nt, Pr, \varepsilon$.

Rd	Nb	Nt	Pr	$Re_x^{-1/2}Nu_x$	
				$m = -0.5$	$m = 0.5$
0.1	0.3	0.7	0.7	0.0594	0.0598
0.2				0.0612	0.0609
0.3				0.0668	0.0671
	0.4			0.0538	0.0534
	0.5			0.0393	0.0397
	0.6			0.0244	0.0248
		0.5		0.0581	0.0584
		0.4		0.0699	0.0702
		0.3		0.0793	0.0796
			0.7	0. 0824	0. 0825
			1.1	0.0984	0.0987

TABLE 4: Numerical values of $Re_x^{-1/2}Sh_x$ with numerous variables of Nb, Nt, Pr, Sc.

Pr	Sc	κ	Nb	Nt	$Re_x^{-1/2}Sh_x$
0.5		2.3	0.4	0.1	0.8429
0.6					0.3218
0.7					1.0624

TABLE 4: Continued.

Pr	Sc	κ	Nb	Nt	$\mathrm{Re}_x^{-1/2}Sh_x$
	0.8				1.9074
	0.9				1.1671
	1.0				1.0741
		2.4			1.1092
		2.5			1.1425
		2.6			1.1770
			0.3		1.1779
			0.4		1.1785
			0.5		1.1810
				0.2	1.4161
				0.3	1.4814
				0.4	1.4918

TABLE 5: Numerical values of $\mathrm{Re}_x^{-1/2}Nh_x$ with numerous variables of Nb, Pe, Lb, ϖ.

Lb	Pe	ϖ	Nb	$\mathrm{Re}_x^{-1/2}\mathrm{Nh}_x$
0.9	0.9	0.9	0.7	2.0658
1.				2.0428
1.1				2.0206
	1.0			2.3002
	1.			2.4351
	1.1			2.5981
		1.1		2.9703
		1.2		3.1641
		1.3		3.5637
			0.3	3.1072
			0.4	3.8628
			0.5	3.9162

TABLE 6: List of symbols.

Expression	Name	Unit
Re	Local Reynolds number	Dimensionless
t	Time	Sec
δ	Deborah number	Dimensionless
M	Magnetic parameter	Dimensionless
m	Power index number	Dimensionless
A	Unsteady parameter	Dimensionless
Nb	Brownian motion parameter	Dimensionless
Nt	Thermophoresis parameter	Dimensionless
Pr	Prandtl number	Dimensionless
$R\,d$	Radiation parameter	Dimensionless
Sc	Schmidt number	Dimensionless
Lb	Bioconvection Lewis number	Dimensionless
Pe	Bioconvection Peclet number	Dimensionless
ε	Heat source/sink parameter	Dimensionless
κ	Chemical reaction parameter	Dimensionless
C_f	Skin friction coefficient	Dimensionless
Nu_x	Nusselt number	Dimensionless
Sh_x	Sherwood number	Dimensionless
Nh_x	Microorganism density number	Dimensionless
f	Dimensionless velocity profile	Dimensionless
θ	Dimensionless temperature profile	Dimensionless
ϕ	Dimensionless concentration profile	Dimensionless
N	Dimensionless microorganism profile	Dimensionless
ϖ	Microorganism concentration difference parameter	Dimensionless
η	Similarity variable	Dimensionless

TABLE 6: Continued.

| Expression	Name	Unit
$\widehat{u}, \widehat{v}$	Components of velocity along x, y direction	ms^{-1}
τ	Ratio of the effective heat capacity	Dimensionless
υ	Kinematic viscosity	$m^2 s^{-1}$
a	Stretching rate	s^{-1}
ρ	Density	kgm^{-1}
C_p	Specific heat	$Jkg^{-1}K^{-1}$
D_B	Brownian diffusion coefficient	$m^2 s^{-1}$
D_T	Thermophoretic diffusion coefficient	$m^2 s^{-1}$
D_m	Microorganism's diffusion coefficient	$m^2 s^{-1}$
B_o	Constant magnetic field	$kgs^{-2}A^{-1}$
$\widehat{C}$	Concentration	kgm^{-3}
$\widehat{C}_\infty$	Ambient concentration	kgm^{-3}
$\widehat{C}_w$	Surface concentration of nanoparticles	kgm^{-3}
k	Thermal conductivity	$mkgs^{-3}K^{-1}$
$\widehat{T}$	Temperature	K
$\widehat{T}_\infty$	Ambient temperature	K
$\widehat{T}_w$	Wall temperature	K
$h(t)$	Coefficient of heat transfer	$W\, m^{-2}K^{-1}$
$\widehat{\chi}$	Microorganism's profile	Dimensionless
$\widehat{\chi}_w$	Surface concentration of microorganisms	kgm^{-3}
$\widehat{\chi}_\infty$	Ambient concentration of microorganisms	kgm^{-3}
W_c	Maximum cell swimming speed	ms^{-1}
x, y	Cartesian coordinates	m
σ	Electrical conductivity	$S^3 m^2\, kg^{-1}$
u_w	Velocity of the sheet	ms^{-1}
S_G	Local volumetric entropy generation rate	$Wm^{-3}K^{-1}$
Ns	Entropy generation	Dimensionless
Be	Bejan number	Dimensionless
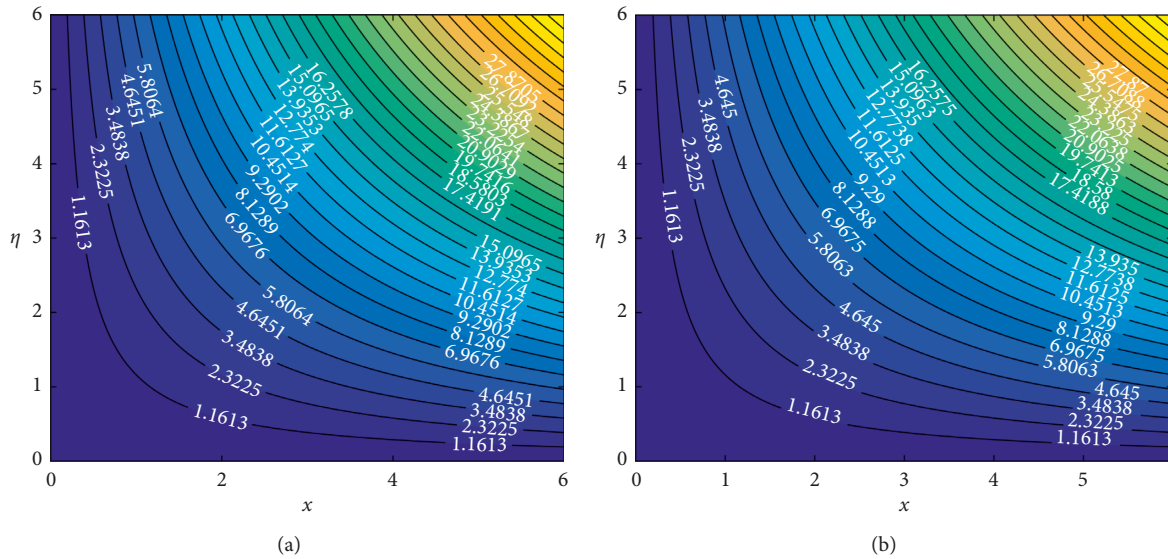
FIGURE 16: Streamlines for (a) Unsteady flow. (b) Steady flow.

escalates when escalating the vales of *Pe* and its downturns for enriching the *Lb* quantity.

Numerical estimation of drag friction for Re, δ and *M* has been shown in Table 2 for dilatant and pseudo-plastic cases. It is noticed that the drag friction diminishes when rising the Re & δ values in the pseudo-plastic case and it is elevated in the dilatant case. In Addition, the drag friction

slumps for a higher quantity of *M* in both cases. Table 3 presents the numerical values of Rd, Nb, Nt, Pr on Nusselt number for $m = -0.5$ and $m = 0.5$. From this table we obtain Rd, *Nt*, Pr have an increasing tendency and the opposite behaviour is found for Nb in both cases. Table 4 provides the consequences of Pr, Sc, κ, *Nb* and *Nt* on the Sherwood number and found that the Sherwood number mounts when
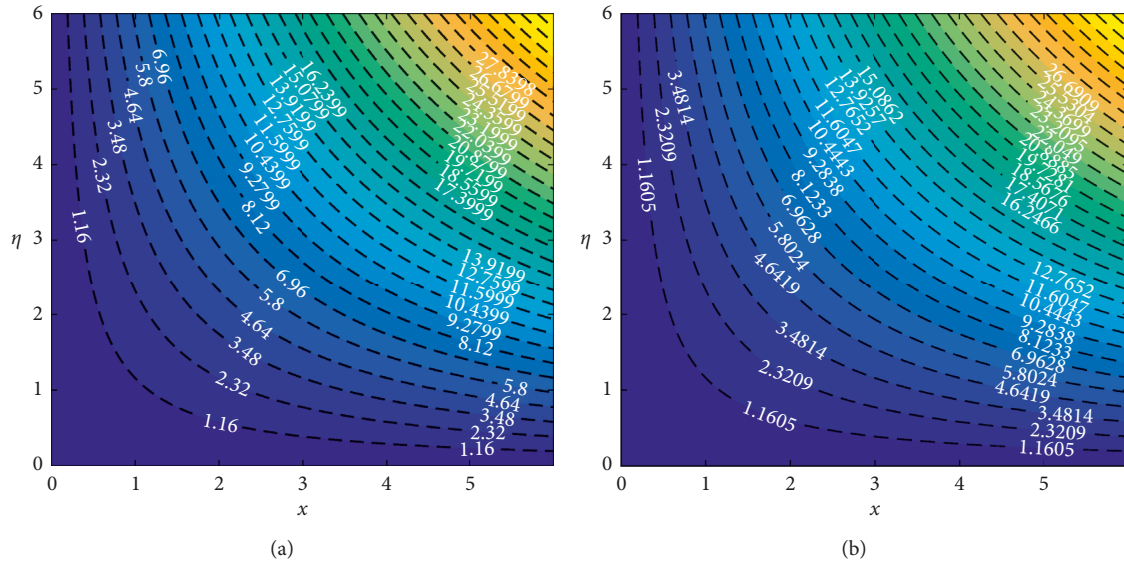
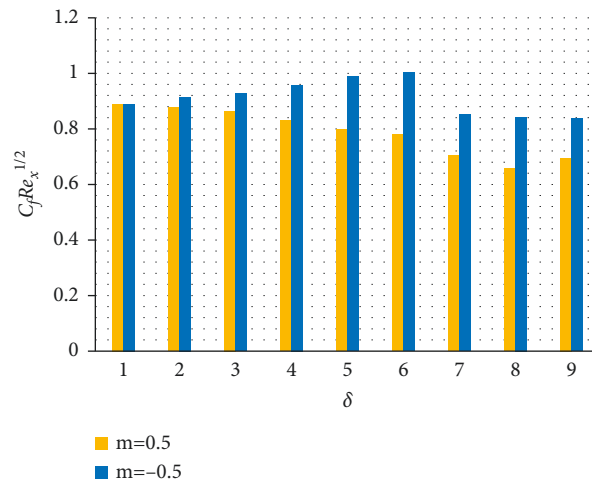FIGURE 17: Streamline for (a) $m = -0.3$ and (b) $m = 0.3$.
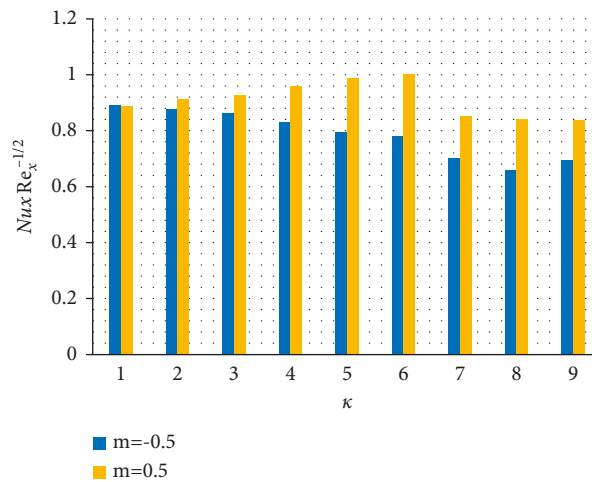

FIGURE 18: Bar graph for skin friction.

FIGURE 19: Bar graph for Nusselt number.

improving the Pr, κ, *Nb* and *Nt* values and its downfalls when larger quantity of Sc values. The impact of Le, Pe, ω and *Nb* on motile density was displayed in Table 5. It is seen that the motile density progress when elevating the Pe, ω and Nb values and it depresses when higher values of Le. Table 6 provides the list of symbols in our analysis. The flow line for steady flow 16(a), unsteady flow 16(b), pseudo-plastic 17(a) and dilatant 17(b) was presented in Figures 16(a), 16(b) and 17(a), 17(b). Figures 18 explains the skin friction coefficient for different values of δ for dilatant and pseudo-plastic cases. It is found that pseudo-plastic has a more pronounced than the dilatant case. The Nusselt number variations for different values of κ for dilatant and pseudo-plastic cases. It is seen that the higher heat transfer gradient attains in pseudo-plastic case than the dilatant case.

5. Conclusion

In this article, the influence of numerical simulation of MHD flow of Sutterby nanofluid with thermal radiation and heat source/sink has been investigated. Entropy production is also considered. The transmuted ODEs are obtained numerically through bvp4c. By this simulation, we have revealed the influence of emerging parameters on the flow of entropy generation and chemical reaction effects with thermal radiative for time-dependent MHD of Sutterby fluid past stretching surface. This investigation can be enlarged for Ree-Eyring fluid, Williamson fluid, and generalized fluid model. Some precise conclusions which have been produced from this research are given as follows.

   (i) Velocity profile is reducing while temperature, entropy generation, and Bejan number accelerated due to the larger value of the Deborah number for $m < 0$.

   (ii) The velocity of fluid mounted whereas temperature, entropy generation, and Bejan number declined due to the larger value of the Deborah number for $m > 0$.

   (iii) A higher value in *Pr* causes the reduction in the temperature profile.

   (iv) Increases in the Deborah number for heat flow result in a decrease in the temperature profile while increasing the heat source/sink parameter.

   (v) Skin friction coefficient augments for ($m < 0$, $m > 0$) but reduced the Nusselt number.

Data Availability

The raw data supporting the conclusions of this article will be made available by the corresponding author without undue reservation.

Conflicts of Interest

The authors declare that they have no conflicts of interest.

Authors' Contributions

All authors listed have made a substantial, direct, and intellectual contribution to the work and approved it for publication.

References

[1] J. L. Sutterby, "Laminar converging flow of dilute polymer solutions in conical sections: Part I. Viscosity data, new viscosity model, tube flow solution," *AIChE Journal*, vol. 12, no. 1, pp. 63–68, 1966.

[2] R. L. Batra and M. Eissa, "Helical flow of a Sutterby model fluid," *Polymer - Plastics Technology & Engineering*, vol. 33, no. 4, pp. 489–501, 1994.

[3] K. Gangadhar, T. Kannan, N. S. L. V. Narasimharao, B. Rushi Kumar, and G. Sakthivel, "Thermo diffusion effects on MHD casson fluid flow over non-flatness stretching surface: keller box method," *International Journal of Ambient Energy*, vol. 42, no. 4, pp. 374–382, 2018.

[4] S. Bilal, M. Sohail, R. Naz, and M. Y. Malik, "Dynamical and optimal procedure to analyse the exhibition of physical attribute imparted by Sutterby magneto nano fluid in Darcy medium yield by axially stretched cylinder," *Canadian Journal of Physics*, vol. 98, 2019.

[5] R. Saif-ur-Rehman, N. A.Mir, M. Farooq et al., "Analysis of thermally stratified flow of Sutterby nanofluid with zero mass flux condition," *Journal of Materials Research and Technology*, vol. 9, no. 2, pp. 1631–1639, 2020.

[6] M. I. Khan, H. Waqas, U. Farooq, S. U. Khan, Y.-M. Chu, and S. Kadry, "Assessment of bioconvection in magnetized Sutterby nanofluid configured by a rotating disk: a numerical approach," *Modern Physics Letters B*, vol. 35, no. 12, Article ID 2150202, 2021.

[7] M. Sohail and R. Naz, "Modified heat and mass transmission models in the magnetohydrodynamic flow of Sutterby nanofluid in stretching cylinder," *Physica A: Statistical Mechanics and Its Applications*, vol. 549, Article ID 124088, 2020.

[8] R. Su, N. A. Mir, M. S. Alqarni, M. Farooq, and M. Y. Malik, "Analysis of heat generation/absorption in thermally stratified Sutterby fluid flow with Cattaneo-Christov theory," *Microsystem Technologies*, vol. 25, pp. 3365–3373, 2020.

[9] L. P. Usman and A. Ghaffari, "Heat and mass transfer in a steady flow of Sutterby nanofluid over the surface of a stretching wedge," *Physica Scripta*, vol. 96, Article ID 065003, 2021.

[10] M. M. Bhatti, S. Jun, C. M. Khalique, A. Shahid, L. Fasheng, and M. S. Mohamed, "Lie group analysis and robust computational approach to examine mass transport process using Jeffrey fluid model," *Applied Mathematics and Computation*, vol. 421, Article ID 126936, 2022.

[11] K. Loganathan, S. Sivasankaran, M. Bhuvaneswari, and S. Rajan, "Second-order slip, cross-diffusion and chemical reaction effects on magneto-convection of Oldroyd-B liquid using Cattaneo-Christov heat flux with convective heating," *Journal of Thermal Analysis and Calorimetry*, vol. 136, no. 1, pp. 401–409, 2019.

[12] S. U. S. Choi, "Enhancing thermal conductivity of fluids with nanoparticles," in *Proceedings of the 1995 ASME International Mechanical Engineering Congress and Exposition*, vol. 231, pp. 99–103, San Francisco, January 1995.

[13] J. Buongiorno, "Convective transport in nanofluids," *Journal of Heat Transfer*, vol. 128, no. 3, pp. 240–250, 2006.

[14] S. Islam, A. Khan, W. Deebani, E. Bonyah, N. A. Alreshidi, and Z. Shah, "Influences of Hall current and radiation on MHD micropolar non-Newtonian hybrid nanofluid flow between two surfaces," *AIP Advances*, vol. 10, Article ID 055015, 2020.

[15] T. S. Karthik, K. Loganathan, A. N. Shankar et al., "Zero and nonzero mass flux effects of bioconvective viscoelastic nanofluid over a 3D Riga surface with the swimming of gyrotactic microorganisms," *Advances in Mathematical Physics*, vol. 2021, Article ID 9914134, 2021.

[16] M. Ijaz, M. Ayub, and H. Khan, "Entropy generation and activation energy mechanism in nonlinear radiative flow of Sisko nanofluid: rotating disk," *Heliyon*, vol. 5, p. e01863, Article ID e01863, 2019.

[17] S. M. Alempour, A. A. Abbasian Arani, and M. M. Najafizadeh, "Numerical investigation of nanofluid flow characteristics and heat transfer inside a twisted tube with elliptic cross section," *Journal of Thermal Analysis and Calorimetry*, vol. 140, no. 3, pp. 1237–1257, 2020.

[18] R. E. Abo-Elkhair, M. M. Bhatti, and K. S. Mekheimer, "Magnetic force effects on peristaltic transport of hybrid bio-nanofluid (Au Cu nanoparticles) with moderate Reynolds number: an expanding horizon," *International Communications in Heat and Mass Transfer*, vol. 123, Article ID 105228, 2021.

[19] Z. Sabir, A. Imran, M. Umar et al., "A numerical approach for 2-D Sutterby fluid-flow bounded at a stagnation point with an inclined magnetic field and thermal radiation impacts," *Thermal Science*, vol. 25, pp. 1975–1987, 2021.

[20] F. Ali and A. Zaib, "Unsteady flow of an Eyring-Powell nanofluid near stagnation point past a convectively heated stretching sheet," *Arab Journal of Basic and Applied Sciences*, vol. 26, no. 1, pp. 215–224, 2019.

[21] W. A. Khan, J. R. Culham, and O. D. Makinde, "Combined heat and mass transfer of third-grade nanofluids over a convectively-heated stretching permeable surface," *Canadian Journal of Chemical Engineering*, vol. 93, no. 10, pp. 1880–1888, 2015.

[22] W. Ibrahim and O. Makinde, "Magnetohydrodynamic stagnation point flow of a power-law nanofluid towards a convectively heated stretching sheet with slip," *Proceedings of the Institution of Mechanical Engineers - Part E: Journal of Process Mechanical Engineering*, vol. 230, no. 5, pp. 345–354, 2016.

[23] M. M. Bhatti, M. B. Arain, A. Zeeshan, R. Ellahi, and M. H. Doranehgard, "Swimming of Gyrotactic Microorganism in MHD Williamson nanofluid flow between rotating circular plates embedded in porous medium: application of thermal energy storage," *Journal of Energy Storage*, vol. 45, p. 103511, 2022.

[24] A. Bejan, "A study of entropy generation in fundamental convective heat transfer," *Journal of Heat Transfer*, vol. 101, no. 4, pp. 718–725, 1979.

[25] E. Azhar, Z. Iqbal, and E. N. Maraj, "Impact of entropy generation on stagnation-point flow of Sutterby nanofluid: a numerical analysis," *Zeitschrift für Naturforschung A*, vol. 71, no. 9, pp. 837–848, 2016.

[26] T. Hayat, Z. Nisar, A. Alsaedi, and B. Ahmad, "Analysis of activation energy and entropy generation in mixed convective peristaltic transport of Sutterby nanofluid," *Journal of Thermal Analysis and Calorimetry*, vol. 143, no. 3, pp. 1867–1880, 2021.

[27] K. Loganathan, K. Mohana, M. Mohanraj, P. Sakthivel, and S. Rajan, "Impact of third-grade nanofluid flow across a convective surface in the presence of inclined Lorentz force: an approach to entropy optimization," *Journal of Thermal Analysis and Calorimetry*, vol. 144, no. 5, pp. 1935–1947, 2020.

[28] T. A. Yusuf, F. Mabood, B. C. Prasannakumara, and I. E. Sarris, "Magneto-bioconvection flow of Williamson nanofluid over an inclined plate with gyrotactic microorganisms and entropy generation," *Fluid*, vol. 6, no. 3, p. 109, 2021.

[29] O. D. Makinde and M. S. Tshehla, "Irreversibility analysis of MHD mixed convection channel flow of nanofluid with suction and injection," *Global Journal of Pure and Applied Mathematics*, vol. 13, pp. 4851–4867, 2017.

[30] K. Loganathan and S. Rajan, "An entropy approach of Williamson nanofluid flow with Joule heating and zero nanoparticle mass flux," *Journal of Thermal Analysis and Calorimetry*, vol. 141, no. 6, pp. 2599–2612, 2020.

[31] M. I. Afridi and M. Qasim, "Entropy generation and heat transfer in boundary layer flow over a thin needle moving in a parallel stream in the presence of nonlinear Rosseland radiation," *International Journal of Thermal Sciences*, vol. 123, pp. 117–128, 2018.

[32] A. I. Alsabery, T. Tayebi, A. J. Chamkha, and I. Hashim, "Effect of rotating solid cylinder on entropy generation and convective heat transfer in a wavy porous cavity heated from below," *International Communications in Heat and Mass Transfer*, vol. 95, pp. 197–209, 2018.

[33] M. Goyal and R. Bhargava, "Boundary layer flow and heat transfer of viscoelastic nanofluids past a stretching sheet with partial slip conditions," *Applied Nanoscience*, vol. 4, no. 6, pp. 761–767, 2014.

[34] G. B. C. Mouli, K. Gangadhar, and B. H. S. Raju, "On spectral relaxation approach for Soret and Dufour effects on Sutterby fluid past a stretching sheet," *International Journal of Ambient Energy*, vol. 43, no. 1, pp. 500–507, 2019.